Journal of Nuclear Medicine, published on November 27, 2020 as doi:10.2967/jnumed.120.252460

Ferronostics: Measuring Tumoral Ferrous Iron with PET to Predict Sensitivity to Iron-Targeted Cancer Therapies

Ning Zhao[1], Yangjie Huang[1], Yung-hua Wang[1], Ryan K. Muir[2], Ying-Chu Chen[2], Junnian Wei[1], Nima Hooshdaran[1], Pavithra Viswanath[1], Youngho Seo[1,3], Davide Ruggero[3,4], Adam R. Renslo[2,3]*, Michael J. Evans[1,2,3,]*

[1]Department of Radiology and Biomedical Imaging, University of California, San Francisco, San Francisco, CA 94158.
[2]Department of Pharmaceutical Chemistry, University of California, San Francisco, San Francisco, CA 94158.
[3]Helen Diller Family Comprehensive Cancer Center, University of California, San Francisco, San Francisco, CA 94158.
[4]Department of Urology, University of California, San Francisco, San Francisco, CA 94158.

Corresponding authors:
Name: Michael J. Evans, PhD
Address: 600 16th Street, N572C, San Francisco, CA 94158
Telephone: 415-514-1292
E-mail: michael.evans@ucsf.edu
ORCID: 0000-0003-4947-1316

Name: Adam R. Renslo, PhD
Address: 600 16th Street, N572D, San Francisco, CA 94158
Telephone: 415-514-9698
E-mail: adam.renslo@ucsf.edu
ORCID: 0000-0002-1240-2846

First author:
Name: Ning Zhao, PhD
Address: 600 16th Street, N552
University of California, San Francisco, San Francisco, CA 94158
Telephone number: (415) 514-1292
E-mail: ning.zhao@ucsf.edu
ORCID: 0000-0003-3699-3369

Running title: Iron targeted theranostics for cancer

Financial Support: This study was supported by an American Cancer Society Research Scholar Grant (130635-RSG-1 7-005-01-CCE), the CDMRP Prostate Cancer Program (W81XWH-18-1-0763, W81XWH-16-1-0435, and W81XWH1810754), and National Institutes of Health (R01AI105106).

Word count: 4932

Keywords: Labile iron pool, theranostics, positron emission tomography

ABSTRACT

Background: Although cancer has been known for decades to harbor an insatiable appetite for iron, only recently has the chemistry emerged to exploit this altered state therapeutically, by targeting the expanded cytosolic 'labile' iron pool (LIP), of the cancer cell. The state of the art includes therapies that react with the LIP to produce cytotoxic radical species (in some cases also releasing drug payloads), and molecules that exacerbate LIP-induced oxidative stress to trigger "ferroptosis". Effectively implementing LIP targeted therapies in patients will require biomarkers to identify those tumors with the most elevated LIP, and thus most likely to succumb to LIP targeted interventions. Toward this goal, we tested herein whether tumor uptake of the novel LIP sensing radiotracer ^{18}F-TRX aligns with tumor sensitivity to LIP targeted therapies.

Methods: ^{18}F-TRX uptake was assessed in vivo among ten subcutaneous and orthotopic human xenograft models. Glioma and renal cell carcinoma were prioritized as these tumors have the highest relative expression levels of STEAP3, the oxidoreductase that reduces ferric iron to the ferrous oxidation state, in the Cancer Cell Line Encyclopedia. The antitumor effects of the LIP activated prodrug TRX-CBI, which releases the DNA alkylator cyclopropylbenzindoline (CBI), were compared in mice bearing U251 or PC3 xenografts, tumors with high and intermediate levels of ^{18}F-TRX uptake, respectively.

Results: ^{18}F-TRX showed a wide range of tumor accumulation. An antitumor assessment study showed that the growth of U251 xenografts, the model with the highest ^{18}F-TRX uptake, was potently inhibited by TRX-CBI. Moreover, the antitumor effects against U251 were significantly greater than those observed for PC3 tumors, consistent with the relative ^{18}F-TRX determined LIP levels in tumors prior to therapy. Lastly, a dosimetry study showed that the estimated effective human doses for adult males and females were comparable to those of other ^{18}F-based imaging probes.

Conclusions: We report the first evidence that tumor sensitivity to a LIP targeted therapy can be predicted with a molecular imaging tool. More generally, these data bring a new dimension to the nuclear theranostic model by showing a requirement for imaging to quantify in situ the concentration of a metastable bioanalyte toward predicting tumor drug sensitivity.

INTRODUCTION

All cancer cells have an inescapable need for more iron than normal tissues to support the intense energetic demands that come with indefinite proliferation (*1*). Cancer cells are thought to increase their intracellular supply of ferric iron (Fe^{3+}) primarily by augmenting expression of the transferrin receptor (TFRC), which binds and internalizes circulating holo transferrin (Tf) through endocytosis (Figure 1A). Cancer cells also overexpress the oxidoreductase STEAP3 within lysosomes which enables the reduction of ferric iron to the more soluble and bioavailable ferrous oxidation state (Fe^{2+}). Ferrous iron is subsequently transported into the cytosol—the reservoir of cytosolic ferrous iron making up the "labile iron pool" (LIP)—where it can then be trafficked to ferritin for storage, or to the mitochondria for conversion to the Fe-S cluster and heme cofactors that support essential enzyme functions in the cell (*2*). An expanded LIP however risks oxidative damage from the reactive oxygen species produced via ferrous iron promoted Fenton reactivity with oxygen and hydrogen peroxide. Normal cells thus maintain a modest LIP, in part by storing iron in ferritin or exporting excess iron via ferroportin. To survive with an elevated LIP, cancer cells become especially reliant on cellular defense mechanisms that protect from reactive oxygen species, a state that if perturbed can lead to iron-dependent cell death, or ferroptosis (*3*). Thus, an expanded LIP is emerging as a defining metabolic feature that distinguishes cancer cells from normal cells.

Because no other metal can substitute for iron in biology, it has long been hypothesized that "ferroaddiction" in cancer might be exploited therapeutically (*1*). However, chemical strategies focusing on depriving cancer of ferric iron with chelation therapy or delivering cytotoxic payloads to cancer by targeting TFRC (e.g. Tf-CRM107) were not effectively clinically (*4*). More recently, the emergence of ferrous iron-specific chemistry has enabled a new therapeutic approach that directly target LIP expansion in cancer cells (*5*). This approach draws conceptually from the mechanism of the antimalarial artemisinin, which kills blood stage *Plasmodium falciparum* parasites via reactive intermediates formed following an initial Fenton chemistry with ferrous iron heme (*6*). This reaction yields a heme adduct that can no longer be detoxified by the parasite, resulting in broad oxidative damage to parasite membranes and macromolecules (Figure 1B). The overwhelming clinical success of artemisinin has established that ferrous iron-dependent pharmacology involving the Fenton reaction can be exploited to safely treat disease in humans (including children). Newer synthetic antimalarial 1,2,4-trioxolanes (e.g., artefenomel)

meanwhile inspired the design of LIP-activated trioxolane (TRX) prodrugs like TRX-CBI that are activated by the expanded LIP within cancer cells to produce cytotoxic free radicals while releasing and activating CBI, a potent DNA alkylator (*5, 7*) (Figure 1B). Proof of concept data in preclinical models show that TRX "caging" of therapeutic payloads increases the tolerated doses of many drugs and intratumoral LIP levels efficiently activate the prodrug, releasing the payload to realize potent antitumor effects.

In parallel with these developments, other new approaches for treating cancer by targeting iron dyshomeostasis have emerged within the past 10 years. For example, several groups have developed therapies that exacerbate LIP-associated redox stress and trigger iron dependent cell death, or "ferroptosis." (*3*) These include several mechanistically unrelated drugs, for example, inhibitors of the cystine/glutamate antiporter xCT (e.g. erastin) or biochemical inhibitors (e.g., RSL3) of glutathione peroxidase 4 (GPX4). Moreover, an emerging narrative from several groups suggests a role for ferroptosis in tumor immunology, both as a mechanism by which tumor cells productively respond to immune checkpoint inhibitors and a vector to produce immune stimulatory signaling molecules in the tumor microenvironment (*8, 9*). Lastly, recent data have also shown that inhibiting lysosome function with "autophagy inhibitors" in fact kills cancer cells by provoking acute LIP starvation (*10*). Collectively, these observations highlight the promise of exploiting the LIP for cancer treatment.

One crucial unmet need to address in advance of clinical trials with LIP targeted therapies is a method to measure LIP in the tumors of cancer patients. Indeed, LIP levels in patient tumors have never been quantified, and a biomarker for LIP could be applied prospectively to define which tumors harbor the highest LIP levels and might be especially vulnerable to LIP targeted therapies. The benefit of such a theranostic approach is now well established and in routine clinical use to select patients for endoradiotherapies like Lutathera and Azedra (*11*).

Since ferrous iron rapidly oxidizes once the native cellular environment is disrupted, it cannot be reliably quantified from tumor biopsies. Therefore, we developed a novel radiotracer termed ^{18}F-TRX to quantify LIP in situ with positron emission tomography (PET)(*12*). ^{18}F-TRX is based on the structure of artefenomel, an antimalarial with excellent pharmacokinetics that is currently in phase 2 clinical trials (*13*) (Figure 1C). Upon reaction with the LIP in tissues, ^{18}F-TRX fragments to generate a fluorine-18 labeled carbon centered radical intermediate that crosslinks cellular proteins and becomes sequestered within those cells. Thus, stable cellular accumulation

of fluorine-18 is expected to be proportional to LIP concentration. We recently disclosed imaging data supportive of this mechanism of action in mice by showing that tissue retention of ^{18}F-TRX was responsive to supplementation or withholding of iron (*12*). Herein, we report the first evidence suggesting that ^{18}F-TRX can be applied to identify tumors likely to respond to a LIP targeting drug, and these data bring a new dimension to the nuclear theranostic model by showing the value of quantifying the concentration of a metastable bioanalyte in situ, and thereby predicting tumor drug sensitivity.

METHODS

General methods

Chemicals were purchased and used without further purification. A rabbit polyclonal antibody targeting STEAP3 (cat. no. 17186-1-AP) was purchased from Proteintech. A polyclonal antibody targeting beta-actin (cat. no. 656120) was purchased from Fisher Scientific. Isotopes were produced by the Radiopharmacy at UCSF. All cell lines were purchased from American Type Culture Collections (ATCC) and cultured according to manufacturer's recommendations. Both ^{18}F-TRX and TRX-CBI were prepared according to the previously reported procedures (*5,12*).

FerroFarRed

Cancer cells (10,000/well) were seeded into 96-well clear bottom plates. After 24 hours, the culture medium was removed, and 100 μL of HBSS solution containing FerroFarRed (5 μM) and Hoechst (1 μg/mL) was added into each well and incubated at 37 ºC for 50 min. The solution was removed and replaced with HBSS buffer. The plate was scanned on a fluorescence microscope (Incell 6500). The quantification of fluorescent intensity was determined by the overall fluorescence strength generated by FerroFarRed dye.

Immunoblot

Cells were lysed in RIPA buffer supplemented with protease and phosphatase inhibitor cocktails (ThermoFisher Scientific). The cell lysates (20 μg/sample) were separated by using 4-12% tris acetate gels (Invitrogen). The proteins were transferred to PVDF membranes, blocked

with 5% (w/v) BSA solution, and immunoblotted with anti-STEAP3 antibody (1:1000) or actin (1:4000) for 1 hour at room temperature. The blots were incubated with a secondary antibody coupled to horseradish peroxidase (1:5000) for 30 min and developed using ECL detection reagent (ThermoFisher Scientific) and ultrasensitive film (Biorad).

Animal Studies

All animal experiments were performed under the approval of the Institutional Animal Care and Use Committee at University of California, San Francisco (UCSF). Athymic nu/nu (4−6 weeks) were purchased from Charles River. Cells (1×10^6) were mixed with Matrigel (Corning) and RPMI 1640 medium (1:1 v/v) and implanted into the left leg. Tumors were palpable by 2-4 weeks. Orthotopic glioma tumors were established as previously described (*14*). Ten days post injection, tumor burden was confirmed by MRI and the mice were transferred for PET/CT studies.

For antitumor assessment studies, TRX-CBI was dissolved in A formulation comprising 5/4/1 PEG 400/20% 2-hydroxypropylcylcodextrine in water/DMSO. Mice were treated with TRX-CBI (7.5 mg/kg) or saline via intraperitoneal administration. Tumor volumes were measured with digital calipers and mouse weight were monitored twice weekly.

Small animal PET/CT Imaging

Data were acquired with a Siemens Inveon microPET/CT. For dynamic acquisitions, the mice were anesthetized prior with 1.5 – 2% isoflurane and positioned on the scanner bed, then approximately 30 MBq of ^{18}F-TRX was injected via tail vein in a volume of 100−150 μL per mouse. All PET imaging data were decay corrected, reconstructed with CT-based attenuation correction, and analyzed with AMIDE software. Regions of interest were manually placed to calculate SUVmean data. Dosimetry was calculated as previously reported (*15*).

Biodistribution Studies

Mice were euthanized after radiotracer injection with CO_2 (g) asphyxiation. The blood and tissues were collected, washed, dried, and weighed. The activity of each tissue was measured with a gamma counter. All data was decay corrected and expressed as a percentage of the injected dose per gram of tissue.

Autoradiography

After 90 min post-injection of ^{18}F-TRX, mice were anesthetized and were perfused with cold PBS via cardiac puncture. Tissues were immediately collected, and flash frozen in OCT on dry ice. Tissues were sectioned to 20 μm and mounted on glass slides. The slides were then exposed on a GE phosphor storage screen and developed on an Amersham Typhoon 9400 phosphorimager. The autoradiography images were processed using ImageJ software.

Statistics

An unpaired, two-tailed Student's t test was used to determine statistically significant differences between two treatment arms. Statistically significant differences in animal survival were analyzed with a log rank (Mantel-cox) test. Pearson's correlation was performed using Prism v8.0. In all cases, P values < 0.01 were reported as statistically significant.

RESULTS

We previously demonstrated the feasibility of LIP dependent tumor detection with ^{18}F-TRX using a small pilot group of mouse and human tumor models (*12*). To better understand the dynamic range of ^{18}F-TRX uptake in tumors, we profiled ^{18}F-TRX uptake in a larger panel of ten subcutaneous human tumor xenografts. For this study, we chose to prioritize glioma and renal cell carcinoma, as a comparative analysis of STEAP3 expression levels across cell lines from the Broad Cancer Cell Line Encyclopedia showed these two tumor types to have the highest mean expression, and previous studies have relied on STEAP3 overexpression as a biomarker of iron dyshomeostasis in cancer (Supplemental Figure 1) (*16*). Biodistribution studies at 90 minutes post injection in mice bearing subcutaneous xenografts showed that the tracer uptake ranged from ~5-1 % ID/g (Figure 2A). We compared these data to STEAP3:actin expression levels per tumor type (Figure 2B). A scatter plot showed a trend toward a positive correlation with ^{18}F-TRX uptake in tumors with a Pearson correlation r value of 0.56. However, there were some examples in which relative STEAP3 expression over the tumor panel did not correlate well with relative tumoral uptake of ^{18}F-TRX, and the correlation did not achieve statistical significance (P ~ 0.08, Supplemental Figure 2). We did find that the ^{18}F-TRX data aligned with LIP levels detected using the Fe(II)-activated fluorogenic dye FerroFarRed (*17*), which is activated by a distinct Fe(II)-dependent

reactivity, suggesting that some of the cancer cell lines utilize mechanisms beyond STEAP3 overexpression to expand LIP (Figure 2C).

We next asked if tumors with high avidity for ^{18}F-TRX are sensitive to LIP targeted therapies. For these studies, we tested tumor sensitivity to TRX-CBI, a LIP activated pro-drug that releases the DNA alkylator cyclopropylbenzindoline (*5*). After showing that U251 cells were sensitive to drug in vitro (Supplemental Figure 3), we performed a 35 day antitumor assessment study treating mice bearing subcutaneous U251 xenografts with vehicle or TRX-CBI (7.5 mg/kg, Q4d). Tumor volume was significantly reduced by TRX-CBI compared to vehicle (Figure 3A and Supplemental Figure 3). Moreover, TRX-CBI significantly extended mouse survival, and mice treated with TRX-CBI lived past 40 days, while all mice receiving vehicle were euthanized by day 38 (Figure 3B).

We then asked if tumors with significantly different levels of ^{18}F-TRX uptake had differential sensitivity to TRX-CBI. For this study, we compared tumor responses between the U251 and PC3, as we previously showed that PC3 tumors have significantly lower ^{18}F-TRX uptake (Figure 4A) but subcutaneous PC3 tumors are still highly sensitive to treatment with TRX-CBI (7.5 mg/kg, Q4d) (*5*). Calculating the percent change in tumor volume from day 0 showed that TRX-CBI more potently inhibited U251 tumor growth compared to PC3 (Figure 4B). The differential sensitivity was observed despite both tumors expressing equivalent levels of STEAP3 (Figure 4C and Supplemental Figure 4). Moreover, we tested if the uptake of ^{68}Ga-citrate aligned with tumor sensitivity, as $^{68}Ga^{3+}$ is a ferric iron mimetic that binds to Tf in serum (*18*). Interestingly, PC3 tumors were significantly more avid for $^{68}Ga^{3+}$ than U251, which further underscores the utility and importance of measuring intracellular LIP levels specifically (with ^{18}F-TRX) as opposed to net ferric iron import via $^{68}Ga^{3+}$-Tf (Figure 4C).

Our preclinical data showing that glioma can have sufficiently high LIP levels for targeted drug delivery coincide with recent data indicating that tumors from patients with high grade glioma overexpress STEAP3 and TFRC, and genetically ablating STEAP3 potently inhibits the proliferation and survival of glioma (*16*). Thus, LIP targeting therapies may be particularly well suited to glioma, and to confirm that LIP expansion is detectable with ^{18}F-TRX PET in a more clinically relevant glioma model, we established orthotopic U87 MG tumors in mouse brains. Glioma lesions were visually obvious on PET, and region of interest analysis showed significantly higher ^{18}F-TRX uptake at 90 min post injection compared to involved adjacent white matter

(Figure 5A and 5B and Supplemental Figure 5). Analysis of the radiotracer distribution within the brain with autoradiography showed ^{18}F-TRX uptake within the tumor and low levels in normal brain (Figure 5C).

Lastly, to assess the feasibility of human studies with ^{18}F-TRX, we conducted a rodent dosimetry study to estimate human-equivalent organ absorbed doses and effective doses (Table 1). Dosimetry was calculated by analyzing dynamic, 90 minute PET acquisitions in tumor naïve male and female nu/nu mice. The data were fitted using the EXM module of the OLINDA/EXM version 1.1 package to derive TIACs. Organ doses were estimated using OLINDA version 2.0, and effective doses were computed using ICRP Publication 103 tissue weighting factors implemented in OLINDA version 2.0. In both genders, the effective dose was less than 0.02 mSv/MBq, or the approximate value for a routine PET acquisition with ^{18}F-fluorodeoxyglucose (*19*). The organs receiving the highest absorbed dose were the heart wall, lungs, and liver.

DISCUSSION

Herein, we show that ^{18}F-TRX can distinguish LIP levels among tumors and point to those that might be most likely to respond to LIP targeted therapies. A survey of ten human xenograft models revealed that glioma and renal cell carcinoma harbor a wide range of LIP concentrations. U251, the model with the highest ^{18}F-TRX uptake, was highly sensitive to treatment with TRX-CBI, a LIP activated prodrug. A comparison of the relative antitumor effects conferred by TRX-CBI treatment revealed that U251 responded more durably than PC3 tumors, a human prostate cancer model with approximately two fold lower uptake of ^{18}F-TRX. Since these data suggest a role for LIP targeted therapies in the treatment of glioma, we further tested whether LIP expansion is evident on PET in an orthotopic model of high grade glioma. U87 MG tumors were clearly detectable on PET compared to uninvolved brain tissue. Lastly, a dosimetry study in mice showed the estimated effective doses to humans to be lower than ^{18}F-FDG. Collectively, these observations make a strong case for human translation of ^{18}F-TRX to collect the first ever measurements of LIP in tumors.

The finding that pre-treatment ^{18}F-TRX uptake in tumors is predictive of sensitivity to treatment with a prodrug that requires LIP activation provides an important confirmation that tracer uptake in tumors at extended time points post injection (i.e. 90 minutes) is predominantly if not

entirely due to LIP triggered probe fragmentation and cellular sequestration. On PET, we of course cannot distinguish chemical species to which the radioisotope is attached, and these data provide important clarity to the unavoidable ambiguity as to whether the tumor signal is also in part derived from iron independent tumor retention of unreacted ^{18}F-TRX through an unknown mechanism.

While the relative tumor LIP levels with ^{18}F-TRX could be corroborated with the structurally and mechanistically distinct chemosensor FerroFarRed, relative STEAP3 expression did not always correlate with LIP levels. Tumors that do not overexpress STEAP3 likely utilize alternative mechanisms to expand the LIP, for example overexpressing HAMP to prevent ferrous iron export by ferroportin or liberating iron from cellular ferritin stores. Conversely, PC3 tumors that have high STEAP3 expression, but relatively moderate LIP, may express high levels of ferroportin compared to tumors like U251. More generally, the biological complexity of iron homeostasis suggests that LIP expansion may not be predictable for all tumor types by qualitatively assessing expression levels of a single protein biomarker using immunohistochemistry. Moreover, although it is not clear whether $^{68}Ga^{3+}$ is a STEAP3 substrate, it is a well-established surrogate for ferric iron biodistribution. Thus, our early data showing that relative tumoral uptake of ^{68}Ga-citrate and ^{18}F-TRX do not align suggest that LIP levels may not be easily inferred from measurements of tumoral uptake of ferric iron. All these observations, while preliminary, converge to underscore the potential utility of a "ferronostic" paradigm in which direct measurement of tumoral iron levels with ^{18}F-TRX PET is applied to prospectively identify tumors that might respond to iron targeted therapies. We are currently expanding the scope of this study to treat additional tumor models with TRX-CBI and other LIP activated prodrugs that release payloads mechanistically unrelated to CBI to test this hypothesis more thoroughly.

Finally, iron dysregulation occurs in many human disorders, including neurodegenerative and cardiovascular diseases, and inflammation (*20-22*). Applying ^{18}F-TRX in the respective patient populations to define the extent of LIP expansion in affected tissues will be an important milestone toward understanding the therapeutic potential of LIP targeted therapies beyond oncology. We are currently working to translate ^{18}F-TRX into the clinic to test hypothesis.

CONCLUSIONS

We report the first evidence that tumor sensitivity to a LIP targeted therapy can be predicted with a molecular imaging tool. These data bring a new dimension to the nuclear theranostic model

by showing a requirement for imaging to quantify in situ the concentration of a metastable bioanalyte toward predicting tumor drug sensitivity.

ACKNOWLDGEMENTS

We gratefully acknowledge T. Huynh for technical assistance with small animal PET/CT studies and J. Blecha for assistance with radiochemistry.

DECLARATIONS

RKM, ARR, and MJE are listed as inventors on patent applications describing ^{18}F-TRX and related radiotracers. ARR is co-founder of and advisor to Tatara Therapeutics, Inc.

KEY POINTS

QUESTION: Are tumoral levels of the labile iron pool as measured with ^{18}F-TRX PET a predictive biomarker tumor sensitivity to iron targeted therapies?

PERTINENT FINDINGS: A survey of ^{18}F-TRX uptake in ten human xenograft models identified the glioma model U251 as having the highest level of the labile iron pool. An antitumor assessment study showed the ferrous iron activated prodrug TRX-CBI potently inhibited growth. The antitumor effects were greater than those observed against PC3 tumors, human prostate cancer with ~2 fold lower ^{18}F-TRX uptake.

IMPLICATIONS FOR PATIENT CARE: ^{18}F-TRX is the first translational in vivo imaging probe that can measure labile iron concentrations in tumors, a finding which could evolve into a new theranostic paradigm to identify tumors likely to succumb to iron targeted therapies currently under development.

REFERENCES

1. Torti SV, Manz DH, Paul BT, Blanchette-Farra N, Torti FM. Iron and cancer. *Annu Rev Nutr.* 2018;38:97-125.
2. Kakhlon O, Cabantchik ZI. The labile iron pool: characterization, measurement, and participation in cellular processes(1). *Free Radic Biol Med.* 2002;33:1037-46.
3. Dixon SJ, Lemberg KM, Lamprecht MR, et al. Ferroptosis: an iron-dependent form of nonapoptotic cell death. *Cell.* 2012;149:1060-1072.
4. Weaver M, Laske DW. Transferrin receptor ligand-targeted toxin conjugate (Tf-CRM107) for therapy of malignant gliomas. *J Neurooncol.* 2003;65:3-14.
5. Spangler B, Fontaine SD, Shi Y, et al. A novel tumor-activated prodrug strategy targeting ferrous iron is effective in multiple preclinical cancer models. *J Med Chem.* 2016;59:11161-11170.
6. Meshnick SR. Artemisinin antimalarials: mechanisms of action and resistance. *Med Trop (Mars).* 1998;58(3 Suppl):13-17.
7. Spangler B, Kline T, Hanson J, et al. Toward a ferrous iron-cleavable linker for antibody-drug conjugates. *Mol Pharm.* 2018;15:2054-2059.
8. Friedmann Angeli JP, Krysko DV, Conrad M. Ferroptosis at the crossroads of cancer-acquired drug resistance and immune evasion. *Nat Rev Cancer.* 2019;19:405-414.
9. Wang W, Green M, Choi JE, et al. CD8(+) T cells regulate tumour ferroptosis during cancer immunotherapy. *Nature.* 2019;569:270-274.
10. Weber RA, Yen FS, Nicholson SPV, et al. Maintaining Iron Homeostasis Is the Key Role of Lysosomal Acidity for Cell Proliferation. *Mol Cell.* 2020;77:645-655.
11. Langbein T, Weber WA, Eiber M. Future of theranostics: an outlook on precision oncology in nuclear medicine. *J Nucl Med.* 2019;60(Suppl 2):13S-19S.
12. Muir RK, Zhao N, Wei J, et al. Measuring dynamic changes in the labile iron pool in vivo with a reactivity-based probe for positron emission tomography. *ACS Cent Sci.* 2019;5:727-736.
13. Phyo AP, Jittamala P, Nosten FH, et al. Antimalarial activity of artefenomel (OZ439), a novel synthetic antimalarial endoperoxide, in patients with Plasmodium falciparum and Plasmodium vivax malaria: an open-label phase 2 trial. *Lancet Infect Dis.* 2016;16:61-69.
14. Izquierdo-Garcia JL, Viswanath P, Eriksson P, et al. IDH1 mutation induces reprogramming of pyruvate metabolism. *Cancer Res.* 2015;75:2999-3009.
15. Seo Y, Gustafson WC, Dannoon SF, et al. Tumor dosimetry using [124I]m-iodobenzylguanidine microPET/CT for [131I]m-iodobenzylguanidine treatment of neuroblastoma in a murine xenograft model. *Mol Imaging Biol.* 2012;14:735-742.
16. Han M, Xu R, Wang S, et al. Six-transmembrane epithelial antigen of prostate 3 predicts poor prognosis and promotes glioblastoma growth and invasion. *Neoplasia.* 2018;20:543-554.
17. Hirayama T, Tsuboi H, Niwa M, et al. A universal fluorogenic switch for Fe(ii) ion based on N-oxide chemistry permits the visualization of intracellular redox equilibrium shift towards labile iron in hypoxic tumor cells. *Chem Sci.* 2017;8:4858-4866.
18. Behr SC, Villanueva-Meyer JE, Li Y, et al. Targeting iron metabolism in high-grade glioma with 68Ga-citrate PET/MR. *JCI Insight.* 2018;3: e93999.

19. Boellaard R, O'Doherty MJ, Weber WA, et al. FDG PET and PET/CT: EANM procedure guidelines for tumour PET imaging: version 1.0. *Eur J Nucl Med Mol Imaging.* 2010;37:181-200.
20. James SA, Roberts BR, Hare DJ, et al. Direct in vivo imaging of ferrous iron dyshomeostasis in ageing caenorhabditis elegans. *Chem Sci.* 2015;6:2952-2962.
21. von Haehling S, Jankowska EA, van Veldhuisen DJ, Ponikowski P, Anker SD. Iron deficiency and cardiovascular disease. *Nat Rev Cardiol.* 2015;12:659-669.
22. Wessling-Resnick M. Iron homeostasis and the inflammatory response. *Annu Rev Nutr.* 2010;30:105-122.

FIGURES

Figure 1. Expansion of the labile iron pool is a general feature of cancer and can be targeted for cancer treatment and imaging. A. Schematic representation of how cancer cells can adjust the relative expression levels of iron regulatory proteins to expand the LIP. In general, LIP expansion comes with an increase in the expression of proteins required to import ferric iron and convert it ferrous iron (TFRC, STEAP3, DMT1), and/or a reduction in the machinery cells use to export iron through reduced expression of FPN or increased expression of the FPN1 inhibitory protein HAMP. TFRC = transferrin receptor, DMT1 = divalent metal transporter 1, FPN1 = ferroportin 1, HAMP = hepcidin. **B.** The structure of artemisinin and a carbon-centered radical arising from reaction of the endoperoxide with iron(II)heme in blood-stage *Plasmodium falciparum* parasites, leading to oxidative stress from reactive oxygen species, protein alkylation, and parasite death. Structure of TRX-CBI and the LIP promoted reaction leading to release of cyclobenzindoline (CBI) cytotoxin. **C.** Structures of the antimalarial artefenomel (left) and ^{18}F-TRX (right), a reactivity-based probe to measure the LIP with PET. On exposure to LIP, the 1,2,4-trioxolane reacts to produce a ^{18}F-linked carbon-centered radical which crosslinks biomolecules and is retained within cells.

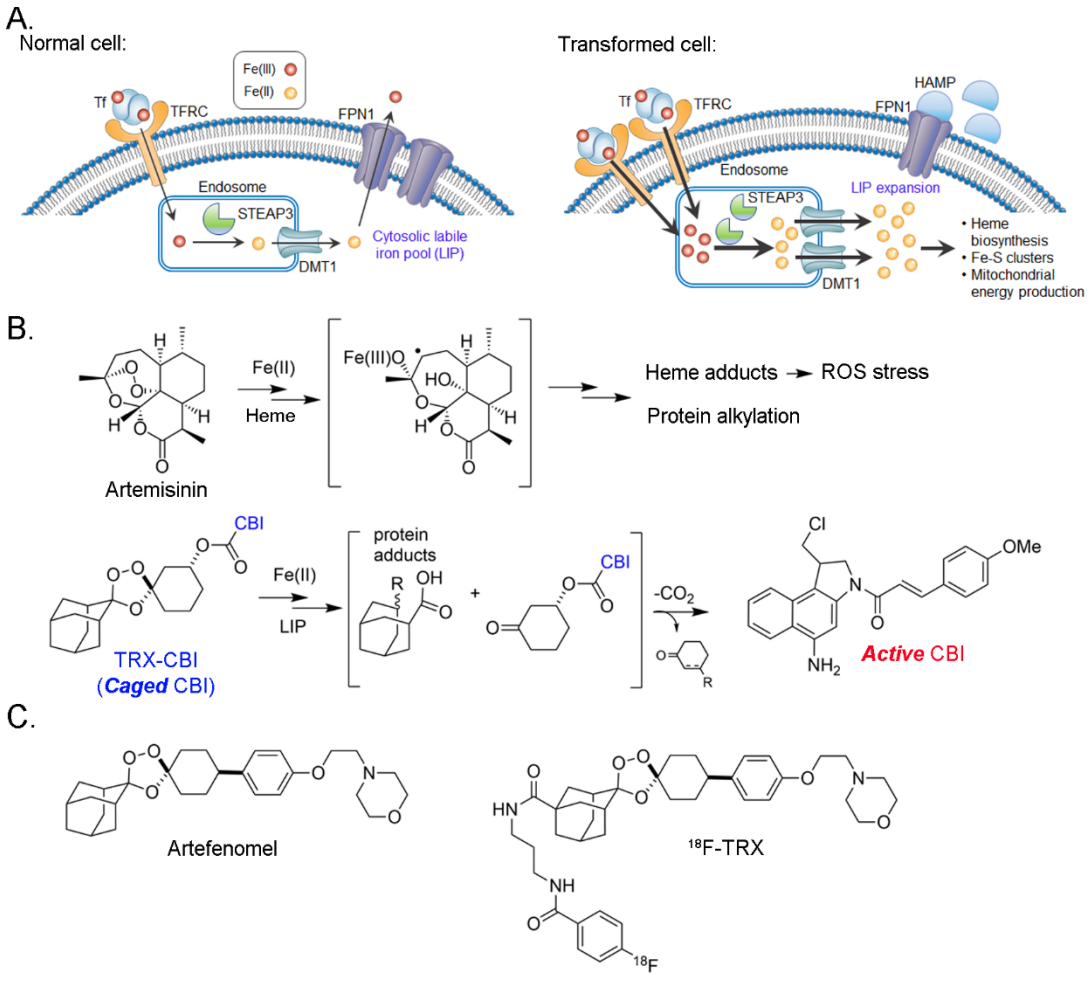

Figure 2. A survey of ^{18}F-TRX uptake in vivo reveals a range of LIP concentrations in human glioma and renal tumors. A. Biodistribution data collected from subcutaneous tumors in nu/nu mice at 90 min post injection of ^{18}F-TRX (n = 4/tumor type). **B.** An immunoblot for STEAP3 shows that protein expression aligns in part with ^{18}F-TRX uptake among those tumors with the highest and lowest radiotracer uptake in vivo. A comparison of the STEAP3:actin ratios (n = 3/cell line) with ^{18}F-TRX uptake per tumor cell indicated a trend toward positive correlation (Pearson r = 0.56), although the correlation did not achieve statistical significance (P ~ 0.08, Supplemental Figure 2). **C.** Immunofluorescence data showing the relative intensity of LIP in A172 and U251 cells in vitro using FerroFarRed. Below the images is shown the quantification of fluorescent intensity. *P<0.01.

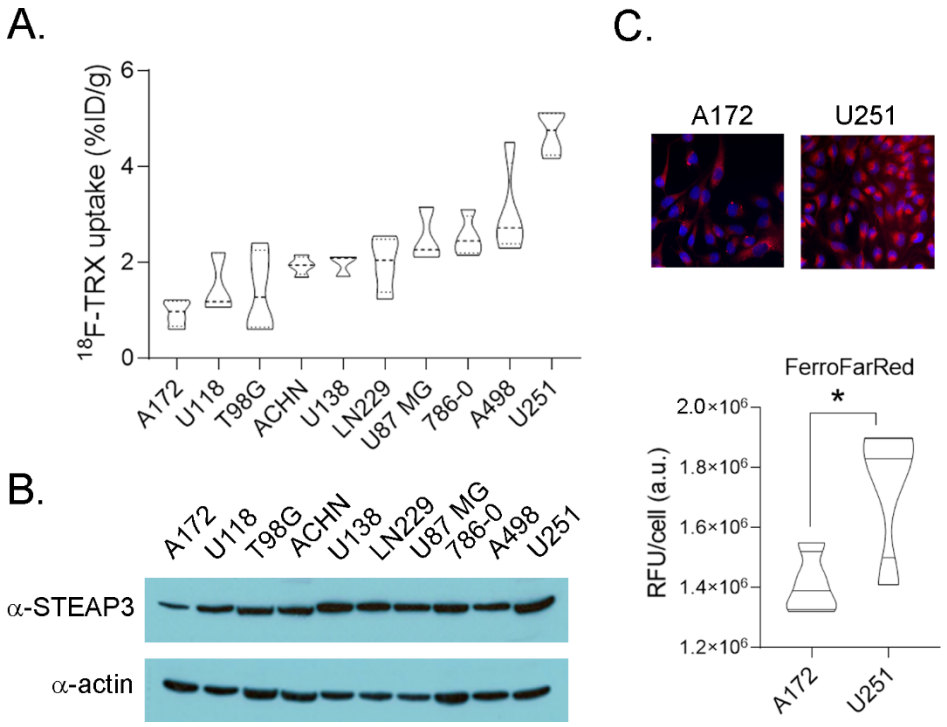

Figure 3. A tumor model with high uptake of ^{18}F-TRX is sensitive to treatment with a LIP targeted therapy. A. Tumor volume data from an antitumor assessment study shows that U251, a human glioma model with the highest ^{18}F-TRX uptake among the tumors surveyed, is responsive to treatment with TRX-CBI. The mice (n = 6/arm) were dosed with vehicle or TRX-CBI at 7.5 mg/kg, Q4d. *P<0.01 **B.** A Kaplan-Meier plot shows the relative survival of mice treated with vehicle versus TRX-CBI. The hazard ratio was 27.

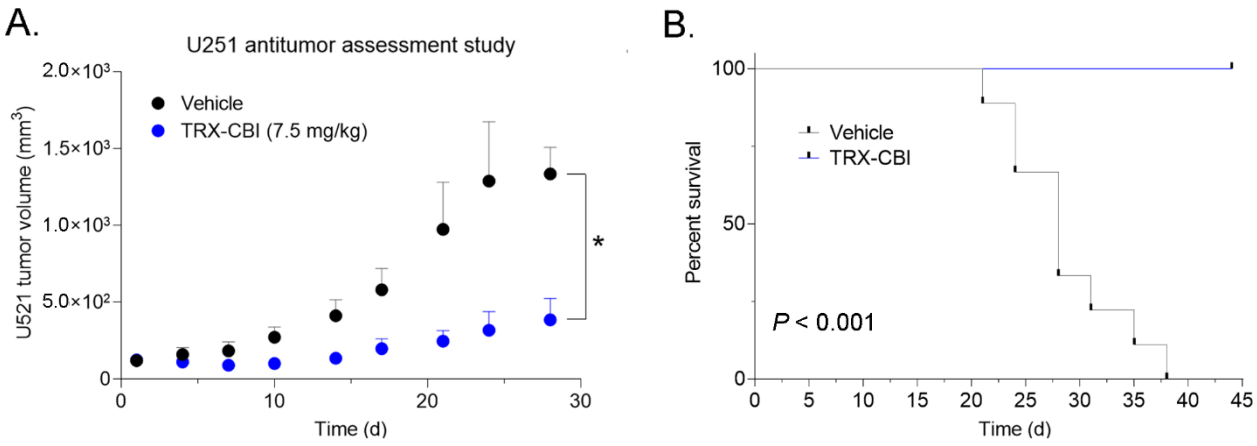

Figure 4. Pre-treatment tumor uptake of ^{18}F-TRX correlates with sensitivity to a LIP activated prodrug. A. At left is shown a plot of the ^{18}F-TRX uptake in nu/nu mice bearing U251 or PC3 tumors, a human prostate cancer model for which we previously conducted an antitumor assessment study with TRX-CBI. At right is shown a plot of the uptake of FerroFarRed in U251 versus PC3 cells, which shows U251 has higher LIP than PC3. Representative fluorescent microscopy images are also shown. *P<0.01 **B.** A plot showing the percent change in PC3 and U251 tumor volume from day 0. The mice were treated with TRX-CBI at 7.5 mg/kg, Q4d. *P<0.01 **C.** At left are representative immunoblot data showing that PC3 and U251 express equivalent STEAP3. Biodistribution data collected 4 hours post injection of ^{68}Ga-citrate in mice bearing subcutaneous PC3 or U251 tumors (n = 4/tumor). Despite higher LIP levels, U251 consumes less $^{68}Ga^{3+}$ bound to transferrin than PC3 tumors. *P<0.01

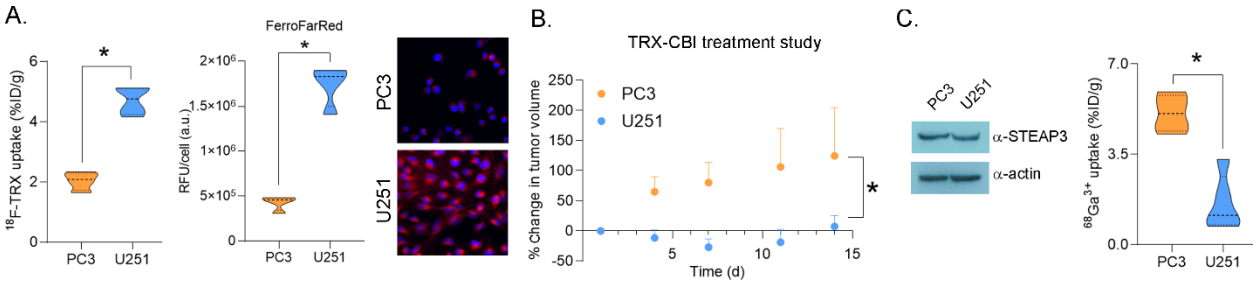

Figure 5. LIP expansion is detectable in an orthotopic glioma model with ^{18}F-TRX. A. ^{18}F-TRX PET/CT data showing radiotracer uptake in a U87 MG tumor (arrow) implanted within the right hemisphere of a mouse brain. The image was acquired at 90 min post injection. **B.** Quantification of ^{18}F-TRX uptake using region of interest analysis of the PET data from mice bearing U87 MG tumors (n = 3). The tumor uptake was compared to uninvolved normal white matter on the contralateral region of the brain. **C.** Digital autoradiography showing the distribution of the radiotracer within a coronal section of the mouse brain. The tissue was stained with H&E and merged with the pseudocolor image of the autoradiography.

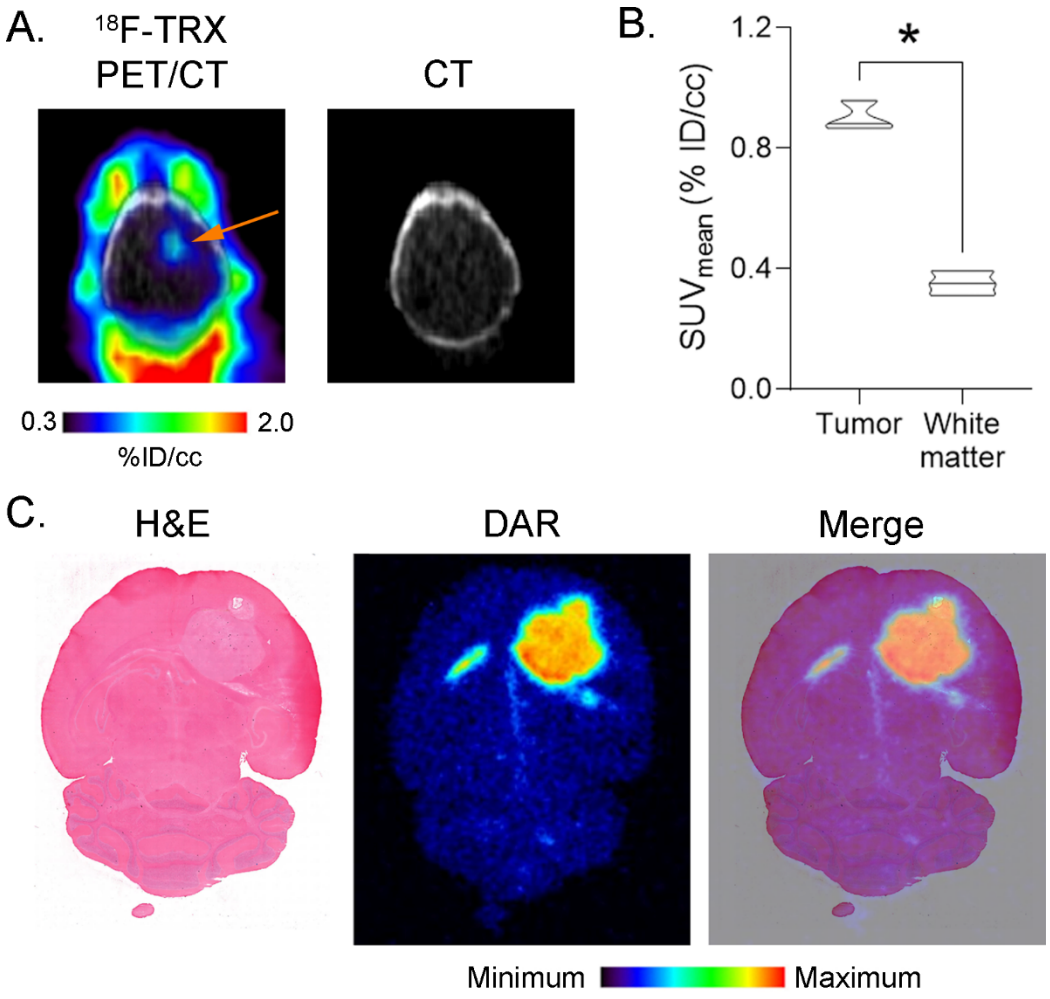

Table 1. A summary of the human equivalent doses for ^{18}F-TRX. These data were calculated using OLINDA version 2.0 using ICRP Publication 103 tissue weighting factors based on a 90 minute dynamic PET acquisition in male or female C57Bl6/J mice.

Organ	**Absorbed dose (mGy/MBq)**	
	Female (60 kg)	**Male (73 kg)**
Adrenals	0.0136 ± 0.0008	0.0141 ± 0.0005
Brain	0.0042 ± 0.0002	0.0030 ± 0.0006
Breast	0.0081 ± 0.0003	
Esophagus	0.0136 ± 0.0004	0.0112 ± 0.0013
Eyes	0.0067 ± 0.0003	0.0073 ± 0.0001
Gallbladder Walls	0.0123 ± 0.0007	0.0161 ± 0.0006
Left Colon	0.0116 ± 0.0004	0.0111 ± 0.0002
Small Intestine	0.0096 ± 0.0004	0.0113 ± 0.0002
Stomach Wall	0.0114 ± 0.0005	0.0117 ± 0.0008
Right Colon	0.0103 ± 0.0005	0.0118 ± 0.0003
Rectum	0.0103 ± 0.0002	0.0111 ± 0.0003
Heart Wall	0.0407 ± 0.0007	0.0206 ± 0.0089
Kidneys	0.0164 ± 0.0011	0.0151 ± 0.0016
Liver	0.0312 ± 0.0026	0.0303 ± 0.0025
Lungs	0.0261 ± 0.0008	0.0138 ± 0.0054
Ovaries	0.0099 ± 0.0003	
Pancreas	0.0129 ± 0.0007	0.0126 ± 0.0006
Prostate		0.0114 ± 0.0004
Salivary Glands	0.0074 ± 0.0003	0.0086 ± 0.0002
Red Marrow	0.0089 ± 0.0003	0.0090 ± 0.0002
Osteogenic Cells	0.0072 ± 0.0003	0.0078 ± 0.0002
Spleen	0.0102 ± 0.0004	0.0102 ± 0.0002
Testes		0.0088 ± 0.0002
Thymus	0.0136 ± 0.0004	0.0108 ± 0.0016
Thyroid	0.0092 ± 0.0003	0.0095 ± 0.0004
Urinary Bladder Wall	0.0201 ± 0.0041	0.0286 ± 0.0050
Uterus	0.0104 ± 0.0002	
Total Body	0.0097 ± 0.0004	0.0096 ± 0.0002
Effective Dose (mSv/MBq)	**0.0126 ± 0.0003**	**0.0103 ± 0.0009**

Graphical Abstract

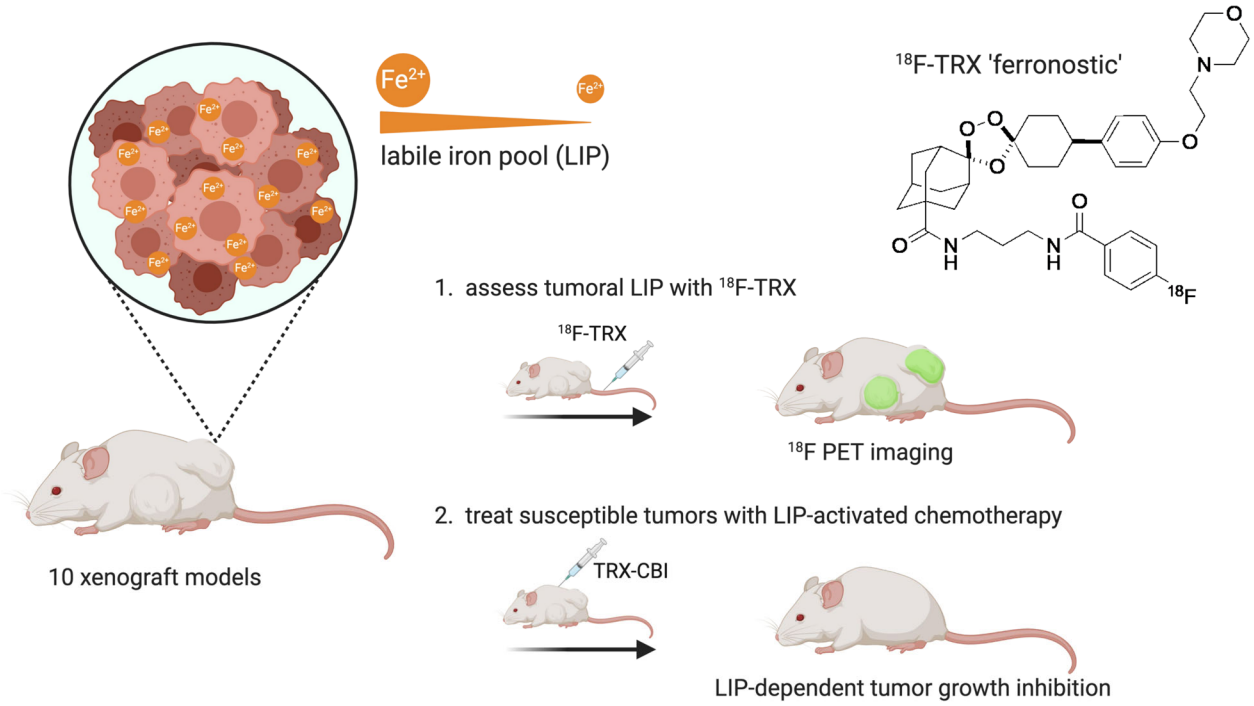

Supplemental Figure 1. A depiction of the relative expression levels of STEAP3 on RNAseq across the cell lines contained within the Broad Cancer Cell Line Encyclopedia. The number of cell lines are indicated parenthetically. Cancers represented by five or fewer cell lines were excluded for clarity. The data were obtained on the open access online portal and exported for depiction here.

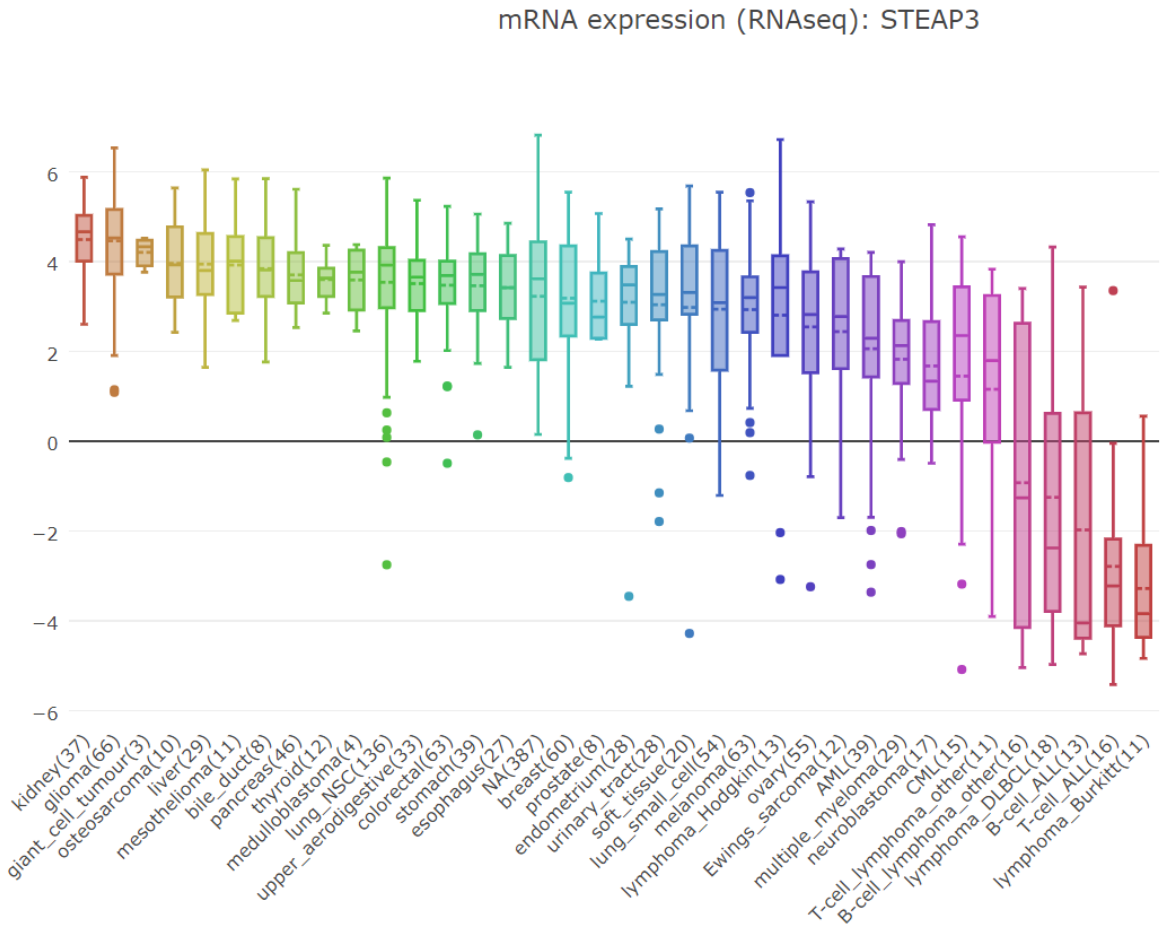

Supplemental Figure 2. A scatter plot showing the correlation between total STEAP3 protein levels and tumoral uptake of ^{18}F-TRX. STEAP3 levels (n = 3) were first normalized to actin, and then the STEAP3:actin ratios were normalized to U251. Data on different blots were normalized using the EKVX "standard". ^{18}F-TRX values were normalized to U251 (n = 4). A linear regression analysis and calculation of Pearson's correlation was performed using Prism v8.0. Shown also are the matched STEAP3:actin and %ID/g values for each cell line. The immunoblot data is shown at bottom.

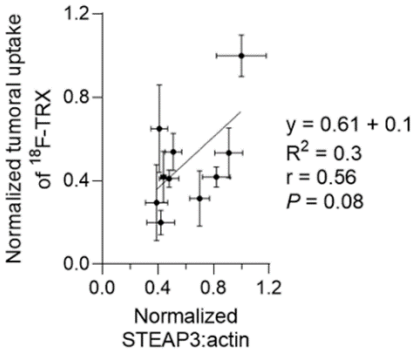

Cell line	Relative STEAP3:actin	Relative %ID/g
T98G	0.39 ± 0.08	0.29 ± 0.09
A498	0.41 ± 0.06	0.65 ± 0.1
A172	0.42 ± 0.1	0.20 ± 0.02
LN229	0.44 ± 0.02	0.41 ± 0.06
ACHN	0.48 ± 0.07	0.41 ± 0.02
786-0	0.51 ± 0.06	0.53 ± 0.04
U118	0.70 ± 0.07	0.31 ± 0.07
U138	0.82 ± 0.1	0.42 ± 0.02
U87 MG	0.91 ± 0.1	0.52 ± 0.06
U251	1.0 ± 0.1	1.0 ± 0.04

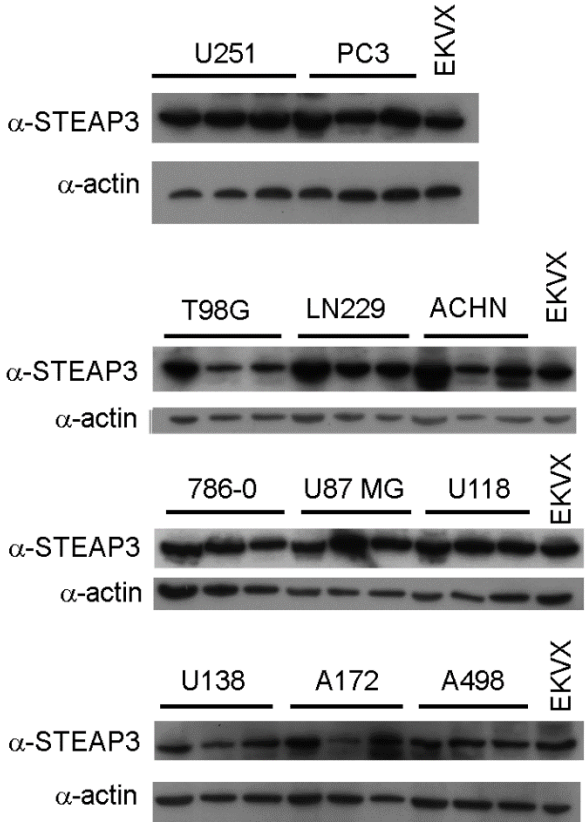

Supplemental Figure 3. In vitro antiproliferation data collected by exposing the indicated cell line with TRX-CBI for four days. The cell numbers were calculated with a Cell Titre Glo assay (Promega) and normalized to the corresponding number for cells exposed to vehicle (3% v/v DMSO). The data are representative of two independent experiments.

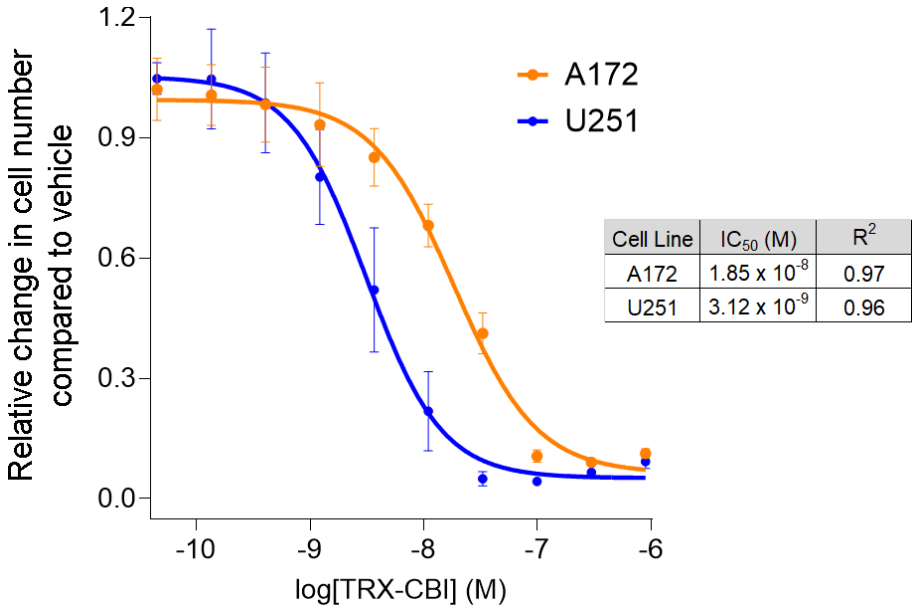

Cell Line	IC_{50} (M)	R^2
A172	1.85×10^{-8}	0.97
U251	3.12×10^{-9}	0.96

Supplemental Figure 3. Tumor volume data for all animals in the TRX-CBI antitumor assessment study. The tumor volume changes are plotted for individual mice.

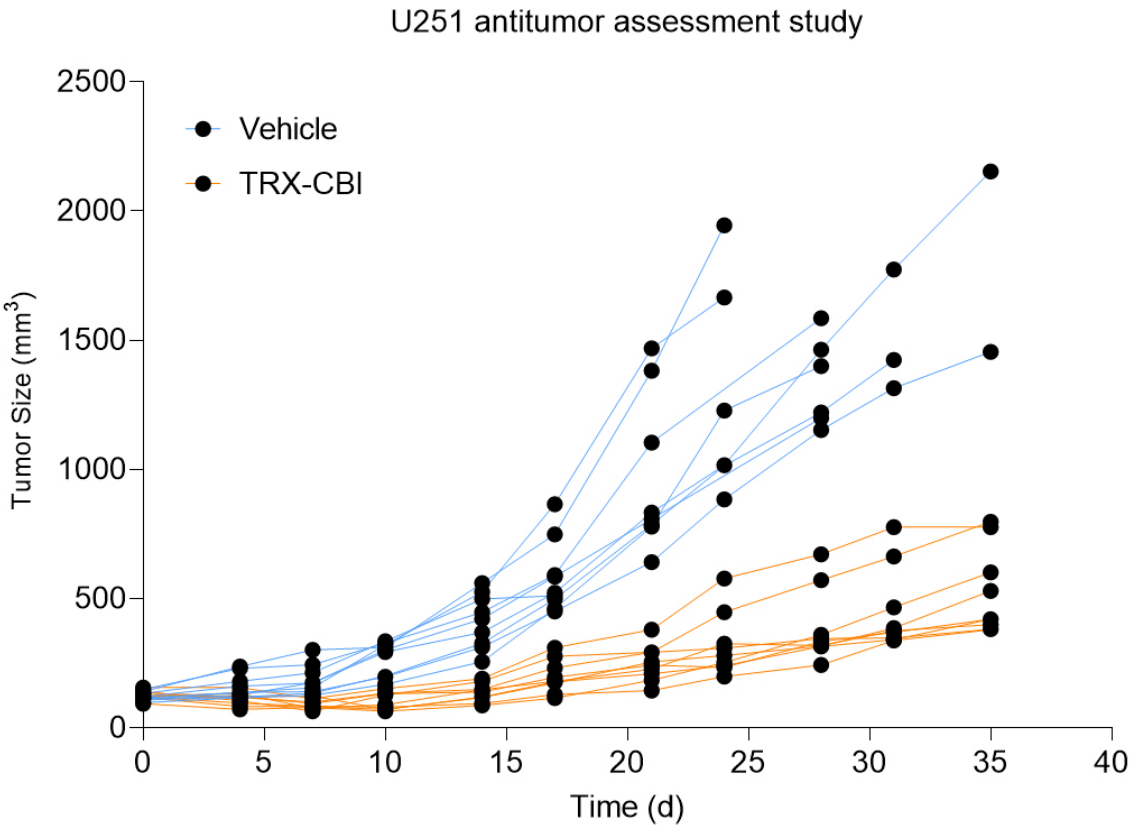

Supplemental Figure 4. Immunoblot data and the corresponding quantification using ImageJ software showing the relative expression of STEAP3 in PC3 and U251 cell lines. The raw immunoblot data are shown in Supplemental Figure 2.

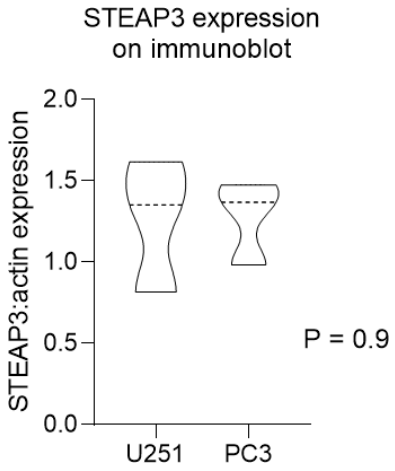

Supplemental Figure 5. A depiction of the region of interests selected for quantification of ^{18}F-TRX in U87 MG orthotopic tumors and normal brain. The size and location of the regions of interest are indicated with orange circles.